Hydrated vanadium pentoxide - reduced graphene oxide hybrid for enhanced performance in aqueous zinc-ion batteries

by

Saptarshi Bhattacharya

B.Sc., St. Xavier's College (Autonomous), Kolkata, 2022
M.Sc., Indian Institute of Technology (Indian School of Mines) Dhanbad, 2024

A THESIS

submitted in partial fulfillment of the requirements for the degree

MASTER OF SCIENCE

Department of Chemistry
College of Arts and Sciences

KANSAS STATE UNIVERSITY
Manhattan, Kansas

2026

Approved by:

Major Professor
Dr Jun Li

Copyright

Abstract

Aqueous zinc-ion batteries (AZIB) are emerging as a safer and more cost-effective alternative to Li-ion batteries for large-scale electrical energy storage due to lower-cost raw materials, greater safety, and the higher ionic conductivity of water as a solvent compared with flammable organic solvents. Despite the high gravimetric specific capacity of zinc (Zn) (820 mAh g^{-1}). The performance of AZIBs is limited by the capacity and stability of the cathode material. Vanadium pentoxide (V_2O_5) is one of the best candidates for cathode material in aqueous zinc-ion batteries. However, the performance of commercially available crystalline α–V_2O_5 is limited by low Zn^{2+} diffusion rate, low electrical conductivity, and structural instability of V_2O_5 nanoparticles due to the tendency to aggregate. These limitations of low diffusion rate can be surpassed by using a hydrated V_2O_5 xerogel structure having a larger interlayer spacing compared to a crystalline α-V_2O_5, due to the presence of intercalated water molecules in between V_2O_5 layers, and low conductivity can be addressed by making a hybrid with conductive carbon material such as reduced graphene oxide (rGO). We have developed a quick and efficient method to synthesize a hybrid material consisting of hydrated V_2O_5 xerogel and reduced graphene oxide (rGO) via microwave irradiation of vanadium (V) triisopropoxideoxide (VTIP) and graphene oxide (GO) at 80°C and 14 bar, which benefits from the increased interlayer spacing of hydrated V_2O_5 and the high electrical conductivity of reduced graphene oxide. In this synthesis method, reaction is completed in less than 10 minutes, offering an advantage over traditional ambient temperature vanadium alkoxide hydrolysis reactions requiring multiple days for the aging process, hydrothermal reaction requiring >10 hours, or melt quenching of solid V_2O_5 requiring heating the V_2O_5 solid to above 700°C. The as-synthesized product (named as-synthesized V_2O_5-rGO) was then annealed at 220 °C and 300 °C for two hours in air atmosphere (named 220 °C annealed V_2O_5-rGO and 300 °C

annealed V_2O_5-rGO respectively) to study the effect of annealing temperature on structure and electrochemical performance. The products were characterized by Raman spectroscopy, X-ray diffraction (XRD), and thermogravimetric analysis (TGA), which revealed that a hybrid material containing hydrated V_2O_5 and rGO was successfully synthesized and revealed the structural and compositional evolution with increasing annealing temperature from hydrated bilayer V_2O_5 to crystalline α-V_2O_5, accompanied by loss of interlayer water molecules. Electrochemical tests (galvanostatic charge-discharge and cyclic voltammetry) using the three products as cathode material coated on Ti discs (along with additive conductive carbon Super P, and polyvinylidene fluoride binder) in coin cells with Zn metal anode give promising results with reversible capacity (calculated with respect to mass of V_2O_5 in hybrid material) of 513, 468 and 304 mAh g^{-1} at 0.4 A g^{-1} for the as-synthesized, 220 °C annealed and 300 °C annealed samples respectively. Despite high specific gravimetric capacity and respectable rate performance, the materials suffer from low cyclic stability and capacity retention, which was not improved on annealing. The as-synthesized material showed the best performance and is a promising candidate for aqueous zinc-ion batteries, and future focus should be on improving cycling stability by optimizing electrolyte, optimizing potential window for charge and discharge, and looking for a deeper understanding of structural degradation on cycling.

Table of Contents

List of Figures

List of Tables

Acknowledgements

I would like to acknowledge Dr. Jun Li for his constant mentorship and support.

I would also like to express my gratitude to the members of the Jun Li Group, Dr. Zahirul Islam Saddam, Vijay Nathan Somasundaram, Dr. Bingun Habarakadage, and Dr. Sanjeev Billa, for their mentorship and help in conducting the experiments.

I would like to thank Dr. Christer B. Aakeroy for letting us use the thermogravimetric analysis facility in his lab.

I would like to thank my supervisory committee members, Dr. Takashi Ito, Dr. Christer B. Aakeroy, and Dr. Gurpreet Singh, for agreeing to be on my committee and for their invaluable time.

Chapter 1 - Introduction

Rising concerns about the environment and climate change have led to a shift in the global energy landscape, prompting nations worldwide to accelerate their transition to renewable energy. By 2030, solar and wind energy are predicted to account for 95% of all new renewable energy capacity.[1] However, renewable energy sources like solar and wind energy are not constant or reliable. This has led to significant challenges for electric grid operators.[2] This has led to the need to create better and more efficient electrical energy storage (EES) systems. Low cost, high reliability, good safety, environmental friendliness, high energy efficiency, long cycle life, and high gravimetric energy and power densities are the most essential for developing the ideal large-scale EES.

In terms of gravimetric energy density, lithium-ion batteries (LIBs) with 240 Wh/kg have a clear advantage. However, the application of LIBs is limited in grid-scale energy storage by their environmental and safety issues. Highly toxic, flammable organic electrolytes are used in LIBs. Additionally, low ionic conductivity and the formation of a solid electrolyte interphase reduce the energy efficiency and power density. And importantly, the cost of LIBs is high not only due to the high cost of lithium but also due to the rigorous cell assembly requirements that keep them moisture and oxygen-free.[3]

Aqueous zinc-ion batteries (AZIBs) stand out as a solution to these problems of large-scale energy storage due to the low cost and high availability of zinc (Zn), its high theoretical specific capacity (820 mAh/g), and its low redox potential (0.763 V vs. standard hydrogen electrode [SHE]), rendering it stable in an aqueous environment.[4] Also, aqueous electrolytes offer high ionic conductivity, greater safety, lower production costs, and environmental friendliness.[5]

Despite the high specific capacity of Zn, the road to industrial production of ZIBs is still restricted by the capacity and stability of its cathode. Vanadium-based oxides have increasingly been studied for application in AZIBs because of tunable multivalent states and lattice spacing, leading to an improved electrochemical performance. Among these V-based oxide materials, V_2O_5 is the most promising cathode. However, owing to the poor electron conductivity and sluggish Zn^{2+} diffusion kinetics of commercially available crystalline α-V_2O_5, its practical application is limited. To boost the performance studies have been conducted on modified cathode materials for V_2O_5-ZIBs, such as, metal-ion pre-intercalated[6], organic molecule intercalated,[7] hydrated V_2O_5[8]

to have increased specific capacity and V_2O_5/C[9] composite to increase rate performance have had respectable results.

In this work, we have synthesized a hybrid material consisting of V_2O_5 xerogel with a bilayer structure with interlayer water molecules, which increases the efficiency with which Zn^{2+} ions can diffuse and get intercalated, and rGO to increase the electronic conductance of the material.

Aqueous Zinc-Ion Batteries

The main mechanism of energy storage in aqueous zinc ion batteries is reversible Zn^{2+} insertion and extraction into the lattice of cathodic host material, during charge and discharge, respectively, while Zn^{2+} ions are extracted and plated on the metallic Zn foil in the anodic compartment. The cathodic and anodic compartments are separated by a porous separator, so that the ions present in the electrolyte can flow between the cathodic and anodic compartments, but there is no direct contact between the cathode and anode materials. This forces the electrons exchanged during the redox reaction to flow through the external circuit, and that current can be used to do work during the discharge cycle.[3]

$$Zn \leftrightarrow Zn^{2+} + 2e^- \quad \text{Anode (Oxidation)} \quad \ldots\ldots (1)$$

$$Zn^{2+} + V_2O_5 + 2e^- \leftrightarrow ZnV_2O_5 \quad \text{Cathode (Reduction)} \quad \ldots\ldots\ldots (2)$$

$$Zn + V_2O_5 \leftrightarrow ZnV_2O_5 \quad \ldots\ldots\ldots (3)$$

However, the performance of AZIB is plagued by the less-understood side reactions like Zn dendrite formation, hydrogen evolution, and formation of passivating hydroxides at the anode[10] and oxide cathode materials dissolution, H^+ co-intercalation at the cathode[11, 12].

The parameters that are evaluated to quantify the performance of such batteries are:

Specific charge and discharge capacities (mAh g^{-1})

$$= \frac{\text{Charge stored during charge or } discharge\ cycle\ (mA\ h)}{Mass\ of\ active\ material\ (g)} = \frac{Current\ (mA) \times\ Time(h)}{Mass\ of\ active\ material\ (g)} \quad \ldots(4)$$

$$\text{Coulombic Efficiency (\%)} = \frac{\text{Discharge capacity}}{\text{Charge capacity}} \times 100\ \% \quad \ldots(5)$$

Background of Synthetic Strategy

Vanadium pentoxide gels have been known for more than a century. These hydrous gels contain water molecules intercalated between the layers. These gels are formed of ribbon-like particles 10nm wide and over 1 μm long. These ribbons consist of polymeric V_2O_5 bilayers with water molecules intercalated between the bilayers. The two close layers are placed about 2.9 Å apart and the interlayer spacing between bilayer is > 10 Å.[13, 14] The intercalated water enhances zinc ion diffusion by increasing the interlayer spacing and by screening the positive charge density of dipositive zinc.

General methods for synthesizing hydrated V_2O_5 gels include sol-gel techniques. One approach is the hydrolysis of vanadium alkoxides at ambient temperature and pressure, resulting in V_2O_5 gel.[15] Another method uses the digestion of vanadium pentoxide powder by hydrogen peroxide to form unstable diperoxo vanadium ions. These ions undergo in-situ oxidation by H_2O_2 and sunsequent self-polymerization to form vanadium pentoxide gels.[16, 17] However, both of these processes have the drawback of taking days to complete the aging process (during which the individual vanadium oxide units join to form the gel structure). Another method is melt-quenching of V_2O_5, which involves melting solid V_2O_5 by heating it at temperatures above 700 °C and pouring the molten V_2O_5 into deionized water.[18] It suffers from the disadvantage of requiring such high temperatures and handling of molten V_2O_5.

One way to facilitate faster reaction completion in the sol-gel method is to perform the reaction in the presence of substrates such as graphene oxide under hydrothermal conditions. This enables preferential nucleation of hydrated V_2O_5 nanoparticles over graphene oxide, and the high pressure and temperature accelerate the aging process.[9,19] However, this process still requires 18 to 20 hours of reaction time. In this work, we have developed a microwave-assisted synthesis mechanism that reduces the reaction time to only 10 minutes.

Vanadium pentoxide gels can be dried to form xerogels or aerogels. Normal drying by heating at ambient pressure creates xerogels, which leads to some collapse of microstructure, and drying under supercritical conditions or freeze-drying leads to the formation of aerogels in which the microstructure is much better preserved.[20] Despite aerogels having higher porosity and surface area, xerogels are comparatively easier to prepare.

Microwave absorption is characterized by dielectric loss and tangent loss (tan delta) values (which is the material's resistance to changes in polarization induced by the microwave's

oscillating electric field; the greater this resistance, the greater is the generation of heat under microwave irradiation), with higher values indicating a stronger heating effect. GO has a high tangent loss value[21], while the chosen solvent, tetrahydrofuran (THF), has a low tangent loss.[22] This ensures that the GO heats up preferentially to the solvent on microwave irradiation, and the hydrolysis reaction takes place preferentially on the surface of the GO, leading to the formation of a hybrid material, and the high temperature and pressure enable the quick completion of the aging process.

In this work, we want to explore the electrochemical properties of the hybrid material and its performance as a cathode for aqueous zinc-ion batteries. Also, it is known that on heating, the hydrated xerogel structure loses intercalated water and changes to crystalline α-V_2O_5 [13, 23] .Thus, we wanted to explore the effect of annealing the hybrid material at different temperatures on its electrochemical performance.

Chapter 2 - Materials and Methods

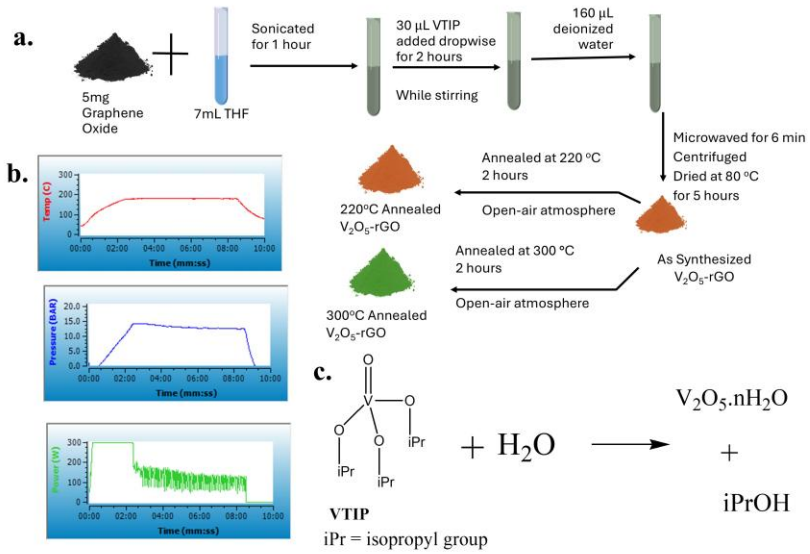

Figure 1 : (a) Schematic representation of the synthesis procedure. (b) Temperature (°C), pressure (bar), and microwave power (W) profiles as a function of reaction time (mm:ss) recorded during the CEM Discover SP microwave synthesis. (c) Chemical equation describing the hydrolysis of vanadium(V) oxytriisopropoxide (VTIP) to form hydrated V_2O_5 ($V_2O_5.nH_2O$).

The schematic diagram for the synthesis is given in Figure 1. To synthesize the V_2O_5-rGO hybrid, 5 mg of GO was dispersed in 7 mL of tetrahydrofuran (THF) in a 10 mL Pyrex glass microwave vessel (CEM, Matthews, NC, USA) and ultrasonicated for 1 hour. After sonication, 30 µL of Vanadium(V) triisopropoxideoxide (VTIP) was added to the suspension in 5 µL aliquots for a duration of 2 hours with vigorous stirring. The addition of VTIP is deliberately slowed to allow sufficient time for VTIP to react with the hydroxyl and carboxylic groups of GO to bond with the GO framework. Then, 160 µL of ultrapure water is added to hydrolyze any remaining VTIP. Then the vessel is placed in the CEM Discover SP microwave reactor (CEM, Matthews, NC, USA) and heated at 180 °C and 13 bar pressure for 6 minutes (the upper pressure limit was set at a safe limit of 18 bar). The resulting product was centrifuged and dried in a two-step process (to prevent aggregation) with an initial overnight drying step at 40 °C to remove excess THF, followed by drying at 80 °C for 5 hours to get the xerogel. The product is denoted as the as-synthesized V_2O_5-rGO. The as-synthesized product is annealed at 220 °C and 300 °C in a tube furnace for 2 hours in air to obtain 220 °C-annealed V_2O_5-rGO and 300 °C-annealed V_2O_5-rGO, respectively. Figure 2.

shows the optical images of the products obtained: a) as-synthesized V_2O_5-rGO (dark green color), 220 °C annealed V_2O_5-rGO (dark green color), and 300 °C annealed V_2O_5-rGO (light green color).

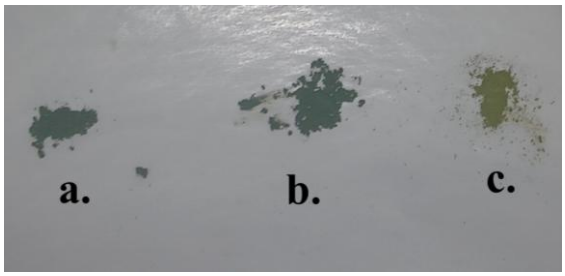

Figure 2 : Optical images of the synthesized products (a) as-synthesized V_2O_5-rGO, (b) 220 °C annealed V_2O_5-rGO, and (c) 300 °C annealed V_2O_5-rGO

Thermogravimetric analysis (TGA) was carried out with a TGA Q50 system (TA Instruments-Waters LLC, New Castle, DE) from room temperature to 700 °C in the air. Raman spectra were obtained using DXR™ Raman microscope (Thermo Fisher Scientific, Madison, WI) with a 532 nm laser at a power of 5 mW, using a 10× objective lens with a slit width of 50 μm. The spectra taken at 4 different spots of the sample were averaged to get the average spectrum for each sample. 16 sample scans and 16 background scans were taken at each spot to reduce the signal-to-noise ratio.

XRD was carried out with D8 ADVANCE diffractometer (Bruker, Germany) within the Chemistry Department using Cu Kα (1.5406 Å) radiation and a 2 mm slit width. The samples were placed on 700 μm-thick single-crystal Si wafers to eliminate background from the plastic sample holder. The scans were taken from $2\theta = 5°$ to $2\theta = 60°$ with a step size of $2\theta = 0.1°$ and a dwell time of 2 s per step.

For electrochemical testing a slurry was prepared with the active material (as-synthesized / 220 ºC annealed / 300 ºC annealed V_2O_5-rGO), Super-P conductive carbon, and PVDF (polyvinylidene fluoride) binder in 70:20:10 ratio by weight. The active material and Super-P were ground together using a mortar and pestle for 10 minutes to create a homogeneous mixture, then a solution of 50 mg/mL of PVDF binder in NMP was added, followed by additional NMP solvent, and the mixture was ground using a mortar and pestle to make a slurry (approximately 450 μL NMP per 50 mg of V_2O_5-rGO material). The homogeneous slurry was brush-coated onto 0.1-mm-thick, 15-mm-diameter titanium (Ti) discs and dried in a vacuum oven at 60 °C overnight. Zn foil

(0.1 mm thick) punched into 15 mm diameter discs was used as an anode, and Whatman GF/F glass microfiber filter papers (Marlborough, MA, USA) cut into 18 mm circles as separators. A 1.2 mm thick stainless-steel spring, a 0.2 mm thick, and a 0.5 mm thick stainless-steel spacer were placed behind the anode to support the electrode structure and maintain internal pressure. The separator was wet with 200 µL of 2.0 M aqueous zinc perchlorate solution, and the stack was assembled into a CR2025 coin-cell casing. Galvanostatic charge discharge was carried out in the cell voltage window of 0.20 - 1.80 V in AZIB tests with a Neware battery testing system (Shenzhen, China) and cyclic voltammetry was carried out in a potential window of 0.20 to 1.8 V at 0.2 mV/s scan rate using CHI 440a electrochemical workstation (CHI instrument, Austin, TX, USA)

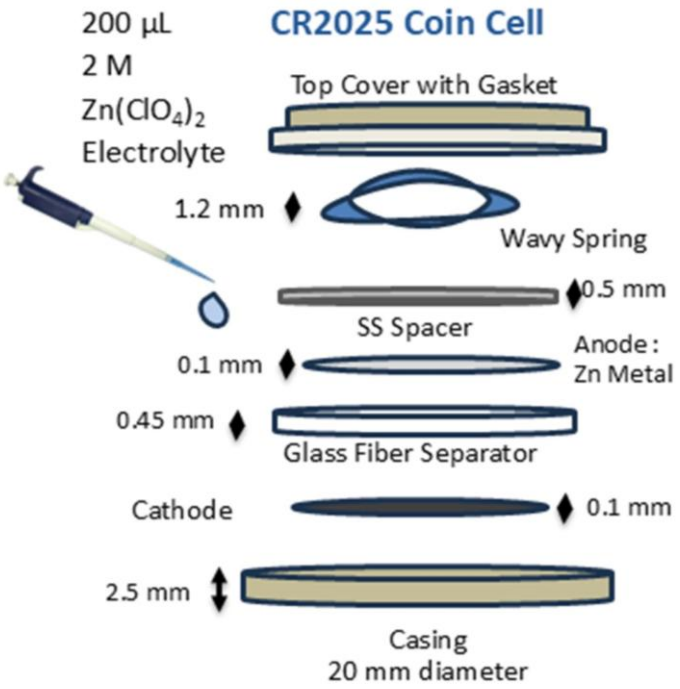

Figure 3 : Schematic of the CR2025 coin cell assembly used for electrochemical testing, illustrating the arrangement of cell components and electrolyte.

Chapter 3 - Results and Discussion

Raman Spectra

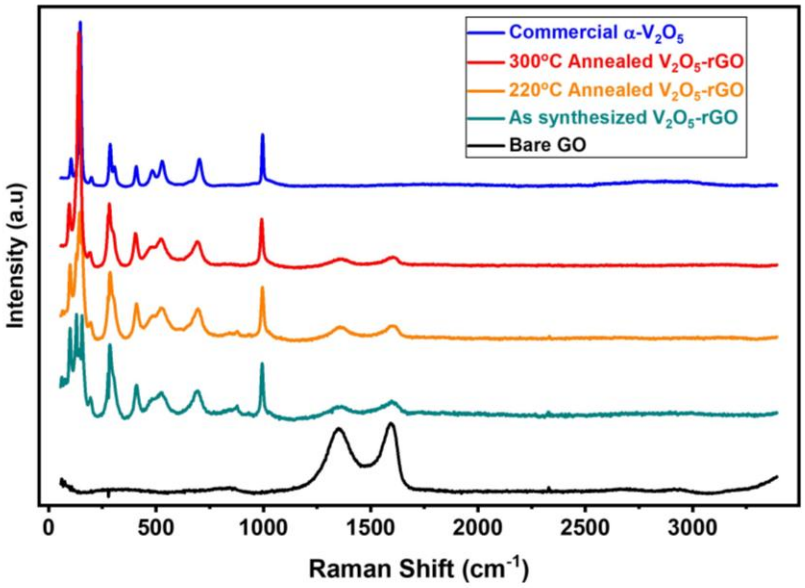

Figure 4 : Raman spectra of V_2O_5–rGO samples: as-synthesized (dark cyan), 220°C annealed (orange), and 300°C annealed (red) compared with commercial α-V_2O_5 (blue) and bare graphene oxide GO (black).

Raman spectroscopy was used to validate the formation of the hybrid material and to understand its structural evolution with increasing annealing temperatures. As seen in Figure 4. the as-synthesized and annealed samples show the characteristic peaks of V_2O_5 (286, 308, 408, 482, 525, 696, and 996 cm^{-1}).[24,25] The peak at 996 cm^{-1} corresponds to V=O stretching, indicative of the presence of the +5 oxidation state of vanadium, which is of low intensity or absent in lower oxidation states. This proves that the main oxide species present in the hybrid material is V_2O_5. The peaks at 525 and 696 cm^{-1} in the as-synthesized and annealed products, corresponding to the stretching modes of triply coordinated oxygen (V_3-O) and doubly coordinated oxygen (V-O-V), respectively, are red-shifted relative to commercial V_2O_5, where they appear at 530 and 702 cm^{-1}, respectively. This could be attributed to strong interaction between V_2O_5 nanoparticles and rGO. [19, 26,] The peaks at 408 and 286 cm^{-1} are assigned to bending vibrations of V=O bonds, and the

ones at 482 and 308 cm^{-1} are assigned to bending vibrations of the doubly coordinated oxygen (V-O-V) and the triply coordinated oxygen (V_3-O), respectively. [24,25].

The peaks at 308 and 482 cm^{-1} appear as shoulders that are almost merged with the neighboring peaks of 286 and 525 cm^{-1}, respectively, in the as-synthesized sample, and as the annealing temperature increases, they become increasingly resolved, with the peaks being distinctly resolved in commercial V_2O_5. This indicates that as annealing temperature increases, long-range order and crystallinity of the material increase.

The peak at 878 cm^{-1} corresponds to out-of-plane O-H deformation of the intercalated water molecules and V-O-H bonds.[27] Its presence in the as-synthesized and 220 °C annealed sample confirms the formation of hydrated V_2O_5. The intensity of this peak decreases from the as-synthesized to the 220 °C annealed sample and disappears in the 300 °C annealed sample, as well as the crystalline α-V_2O_5, indicating that on annealing at 300 °C, most of the interlayer water is removed and the sample is predominantly crystalline V_2O_5.

The peaks at wavenumbers lower than 200 cm^{-1} correspond to lattice vibrations. The peak at 128 cm^{-1} is present in the as-synthesized sample and shows a reduction in intensity upon annealing, consistent with the literature.[23]

X-Ray Diffraction

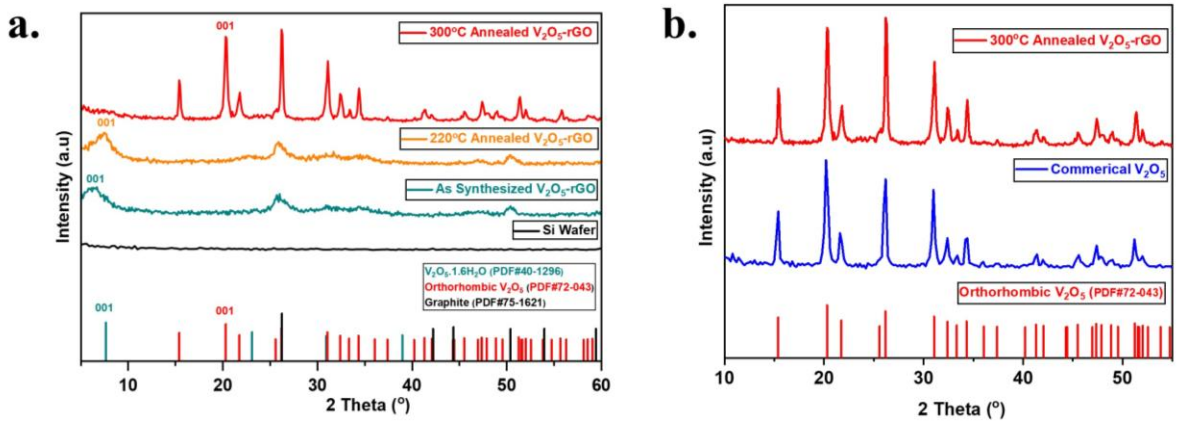

Figure 5 : Powder XRD spectra of V_2O_5-rGO samples (a) as synthesized (dark cyan), 220 °C annealed (orange), and 300 °C annealed (red), and background from Si wafer support with standard patterns of $V_2O_5 \cdot 1.6H_2O$, Orthorhombic α-V_2O_5, and graphite. (b) Comparison between XRD spectra of 300°C annealed (red) and commercial α-V_2O_5 (blue).

The XRD spectra (Figure 5) show how the structure and crystallinity change with annealing temperature. Both the as-synthesized and 220 °C annealed samples exhibit an XRD pattern characteristic of bilayer structure of hydrated V_2O_5.[23] From the (001) peak at 6.56°, the (001) interlayer spacing was calculated to be 13.48 Å for the as-synthesized sample. In the sample annealed at 220°C, the (001) spacing is calculated to be 12.04 Å, corresponding to a 2θ angle of 7.34 °, clearly indicating a reduction of interlayer spacing due to the removal of intercalated water molecules. According to prior literature, the interlayer spacing of 13.48 Å roughly corresponds to 3.5 water molecules per V_2O_5 unit, and 12.04 Å roughly corresponds to 2.5 water molecules per V_2O_5 unit (2.8 Å is the van der Waals radius of a water molecule, which corresponds to one layer of intercalated water, in turn corresponding to two water molecules per V_2O_5 unit).[13]

For the 300 °C annealed sample, the (001) bilayer peak is no longer present, and the diffraction pattern completely matches the orthorhombic α-V_2O_5 phase (commercial V_2O_5 and JCPDS #72-0433), indicating complete conversion of bilayer V_2O_5 to crystalline orthorhombic α-V_2O_5 on annealing at 300 °C. For the 300 ºC annealed sample, the (002) 2θ peak at 20.33 ° corresponds to a d-spacing of 4.37 Å, indicating a completely dehydrated crystalline phase.

The 2θ peaks at 25.97 ° and 25.98 ° for the as-synthesized and 220 °C annealed samples appear in the region of both the second-order diffraction peak of the (001) plane of hydrated V_2O_5 as well as the (002) plane of graphitic carbon layers (JCPDS #75-1621),. However, the ratio of intensity of the observed peaks in this region to the intensity of the (001) peak is too high when compared to XRD spectra of pure hydrated V_2O_5 (without rGO) in the literature. [23,16] Thus, this peak is assigned to the (002) planes of the graphitic carbon layers in rGO. Using Bragg's equation, these 2θ values correspond to an interlayer spacing of 3.43 Å for both the as-synthesized and 220 °C annealed samples, indicating the presence of graphitic carbon phase in rGO for both of those samples.

Thermogravimetric Analysis

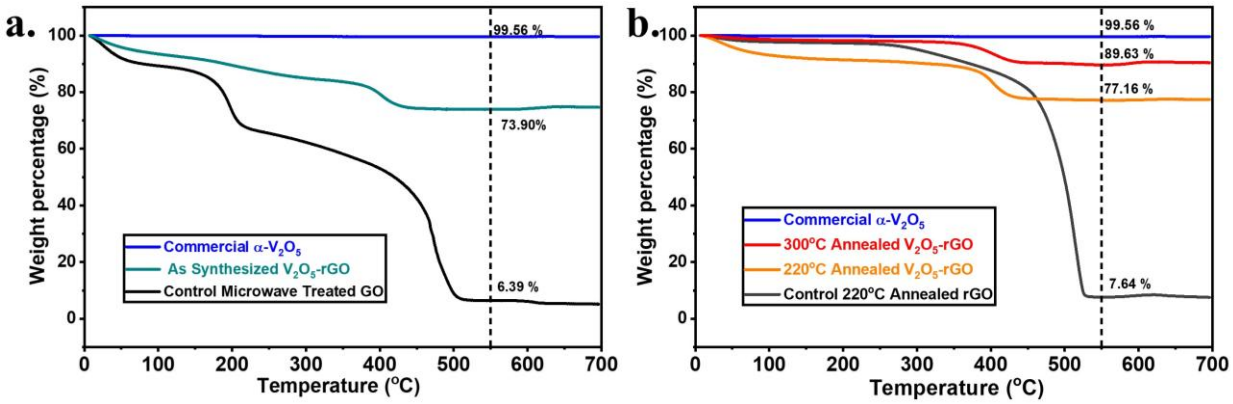

Figure 6 : TGA curves of (a) as-synthesized V_2O_5-rGO (dark cyan), commercial α-V_2O_5 (blue), and microwave-treated GO (black). (b) 220 °C annealed V_2O_5-rGO (orange), 300 °C annealed V_2O_5-rGO (red) commercial α-V_2O_5 (blue), and 220 °C annealed microwave-treated GO (black).

Thermogravimetric analysis was used to estimate the relative composition of the V_2O_5 and rGO present in the as-synthesized and annealed samples. The temperature was ramped from room temperature to 700 ºC at a rate of 10 ºC per minute in a compressed-air atmosphere. Control samples of microwave-treated GO (for as- synthesized V_2O_5-rGO) and microwave-treated GO annealed at 220 °C for 220 °C, and 300 °C annealed V_2O_5-rGO, and commercial α-V_2O_5 were used to find out the relative amount of V_2O_5 and rGO present in the hybrid sample. The curves are shown in Figure 6.

$$Weight\ percent\ of\ rGO\ in\ V_2O_5 - rGO\ hybrid\ + \\ Weight\ percent\ of\ V_2O_5\ in\ V_2O_5 - rGO\ hybrid\ =\ 100\% \quad \ldots\ldots\ldots (6)$$

$$Weight\ percent\ of\ V_2O_5 - rGO\ hybrid\ left\ at\ 550\ °C = \\ [(Weight\ percent\ of\ rGO\ in\ V_2O_5 - \\ rGO\ hybrid\ )\ \times\ (Weight\ percent\ of\ control\ rGO\ left\ at\ 550\ °C)] + \\ [(Weight\ percent\ V_2O_5\ in\ V_2O_5 - \\ rGO\ )\ \times\ (Weight\ percent\ of\ control\ V_2O_5\ left\ at\ 550\ °C\ )] \quad \ldots\ldots\ldots\ldots (7)$$

For microwave-treated GO, the loss of weight between 150 - 200 °C is due to the conversion of GO to rGO by the removal of oxygenated functional groups. Thus, the control sample for 220 °C and 300 °C annealed samples uses microwave-treated GO annealed at 220 °C to remove the oxygenated groups (named as 220 °C annealed rGO); the removal of oxygenated functional groups is confirmed by the absence of significant mass loss up to 300 °C

Loss after 400 °C is due to oxidation of rGO to CO_2, with the 6.39 % (microwave-treated GO) and 7.64 % (220 °C annealed rGO) weight remaining at 550 °C being due to graphitized carbon.[28]

TGA curve of commercial α-V_2O_5 appears as a flat line with negligible loss of mass till 700 °C (99.56 % weight remaining at 550 °C).

For 220 °C annealed and as-synthesized hybrids, the weight loss has a slope and no clear plateau up to 400 °C. This can be attributed to loss of adsorbed water as well as intercalated water, as well as the loss of remaining oxygenated groups from rGO in the as-synthesized sample. This slope is significantly less for the 220 °C annealed sample than for the as -synthesized one, indicating a reduction in the amount of hydration. For 300 °C annealed hybrid, this region shows negligible loss, appearing as an almost flat line very close to the curve for commercial α-V_2O_5, indicating negligible hydration.

In the region, 400 °C to 700 °C, mass loss in the hybrids is due to the removal of rGO as CO_2, resulting in a plateau once all the carbon is removed. The mass percentage remaining at this plateau at 550 °C is used to calculate the relative percentage of V_2O_5 and rGO in the samples. The as-synthesized, 220 °C annealed, and 300 °C annealed samples are found to have 30.53 %, 24.04 %, and 10.80 % rGO and 69.47 %, 75.96%, and 89.20 % V_2O_5, respectively (Table 1). The amount of rGO gets halved from the 220 °C annealed to the 300 °C annealed sample because loss of rGO as CO_2 already starts at 300 °C as seen from the TGA curves of control GO. Thus, annealing the as-synthesized sample at 300 °C for 2 hours removes a significant amount of rGO.

Table 1 : Weight composition of V_2O_5 and rGO in V_2O_5-rGO hybrid samples

Sample	Weight Percent of rGO	Weight Percent of V_2O_5
As Synthesized V_2O_5-rGO	30.53 %	69.47%
220°C Annealed V_2O_5-rGO	24.04 %	75.96 %
300°C Annealed V_2O_5-rGO	10.80 %	89.20 %

Electrochemical Characterization

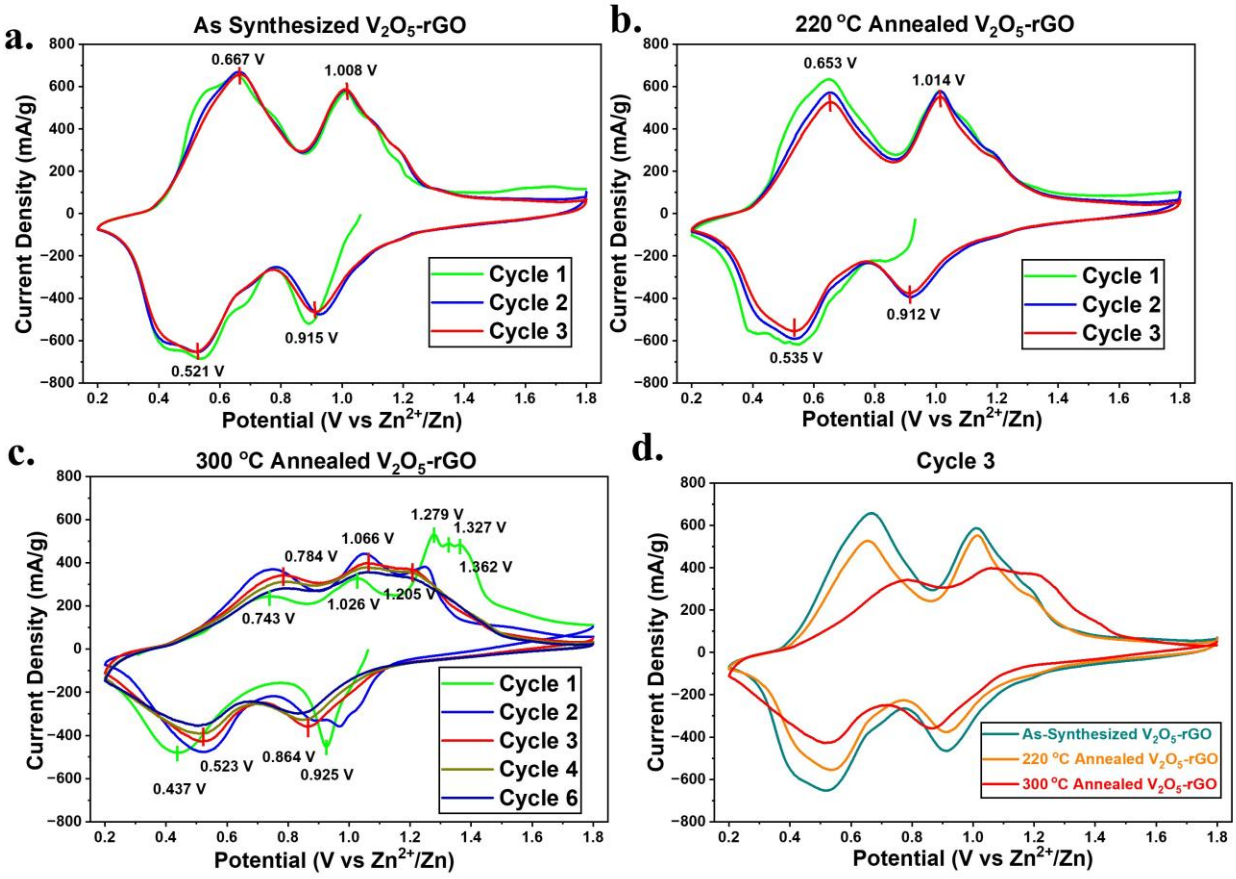

Figure 7 : Cyclic voltammograms (CV) of the V_2O_5-rGO samples as cathodes in AZIB at 0.2 mV/s scan rate (a) as- synthesized, (b) 220 °C annealed, (c) 300 °C annealed. (d) Comparison of the third cycle CV curves of the three samples

Cyclic voltammetry was performed to elucidate the charge-storage mechanism and kinetics of the hybrid cathode materials in aqueous zinc-ion batteries (AZIBs). From Figure 7. we can see that after stabilization, all the samples show two distinct pairs of redox peaks corresponding to the two-step zinc intercalation into V_2O_5.[6] The peak positions and shapes of the curves are almost identical for as-synthesized and 220 ºC annealed samples indicating a similar intercalation mechanism in both materials. This is corroborated by XRD, which shows that they both have an amorphous bilayer structure. The pairs of redox peaks appear at 0.521 V/0.667 V and 0.915 V /1.008 V for as-synthesized V_2O_5-rGO and at 0.535 V/0.653 V and 0.912 V /1.014 V for 220 ºC

annealed V_2O_5 – rGO. Despite the similarities, here still is a significant decrease in peak current on going from as-synthesized to 220 °C annealed sample (as-synthesized : 652 mA g^{-1} / 657 mA g^{-1} and 465 mA g^{-1} / 587 mA $g^{-1}$for 0.521 V/0.667 V and 0.915 V /1.008 V peaks respectively; 220 °C annealed: 555 mA g^{-1}/ 526 mA $g^{-1}$and 376 mA g^{-1} / 552 mA g^{-1} for 0.535 V/0.653 V and 0.912 V /1.014 V peaks respectively). From the relative areas and peak currents, it is evident that the second intercalation step is responsible for more charge storage than the first, and the first deintercalation step is responsible for more charge removal. This is consistent with the fact thatinsertion of the first batch of Zn^{2+} further increases the interlayer spacing , making it easier for the Zn^{2+} of the second intercalation step to enter, and the reverse occurs during deintercalation. The peak-to-peak separation for the two redox peaks is 0.146V and 0.093V for the as-synthesized sample and 0.118 V and 0.102 V for the 220 °C annealed sample, showing lower energy barriers and better reversibility of zinc intercalation and deintercalation.[6,29] Consecutive cycles overlapping show the electrochemical stability of the system.

For the 300 °C annealed V_2O_5-rGO cathode, a few changes are noticed. The first cycle shows two reduction peaks at 0.925 V and 0.437 V, and oxidation peaks at 0.743 V, 1.026 V, 1.279 V, 1.327 V, and 1.362 V. The peaks at 1.279 V, 1.327V, and 1.362 V are assigned to irreversible H^+ intercalation, which occurs as an activation process in crystalline α-V_2O_5 in initial cycles, resulting in its modification to a structure similar to hydrated V_2O_5 which acts as the active cathode material for reversible Zn^{2+} storage in further cycles.[30,31] These peaks shift to a lower potential in second cycle and remain as a small shoulder in the third cycle onwards. The presence of the activation peak further proves that the 300 °C annealed sample is crystalline α-V_2O_5 and no longer hydrated V_2O_5. Considering the third CV cycle for each material, the oxidation peaks are higher and the reduction peaks are lower for 300ºC annealed sample compared to the as-synthesized and the 220 °C annealed hybrids indication lower feasibility of redox reaction and an increased peak-to-peak separation of 0.261 V and 0.202 V and significant broadening of the peak shape demonstrating an increase in energy barrier for the Zn^{2+} intercalation/deintercalation. The difference in peak position between the as -synthesized and 220 °C annealed samples in less than 15 mV and hence, no certain conclusion can be drawn from it as such small variations can arise from difference in electrode uniformity. The corresponding lower peak currents of 427 mA g^{-1}/ 342 mA g^{-1} and 359 mA g^{-1} / 397 mA g^{-1} for the 0.523 V/ 0.784 V and 0.864 V / 1.066 V peaks, which reflect the slower diffusion due to the loss of increased interlayer spacing of the bilayer structure.

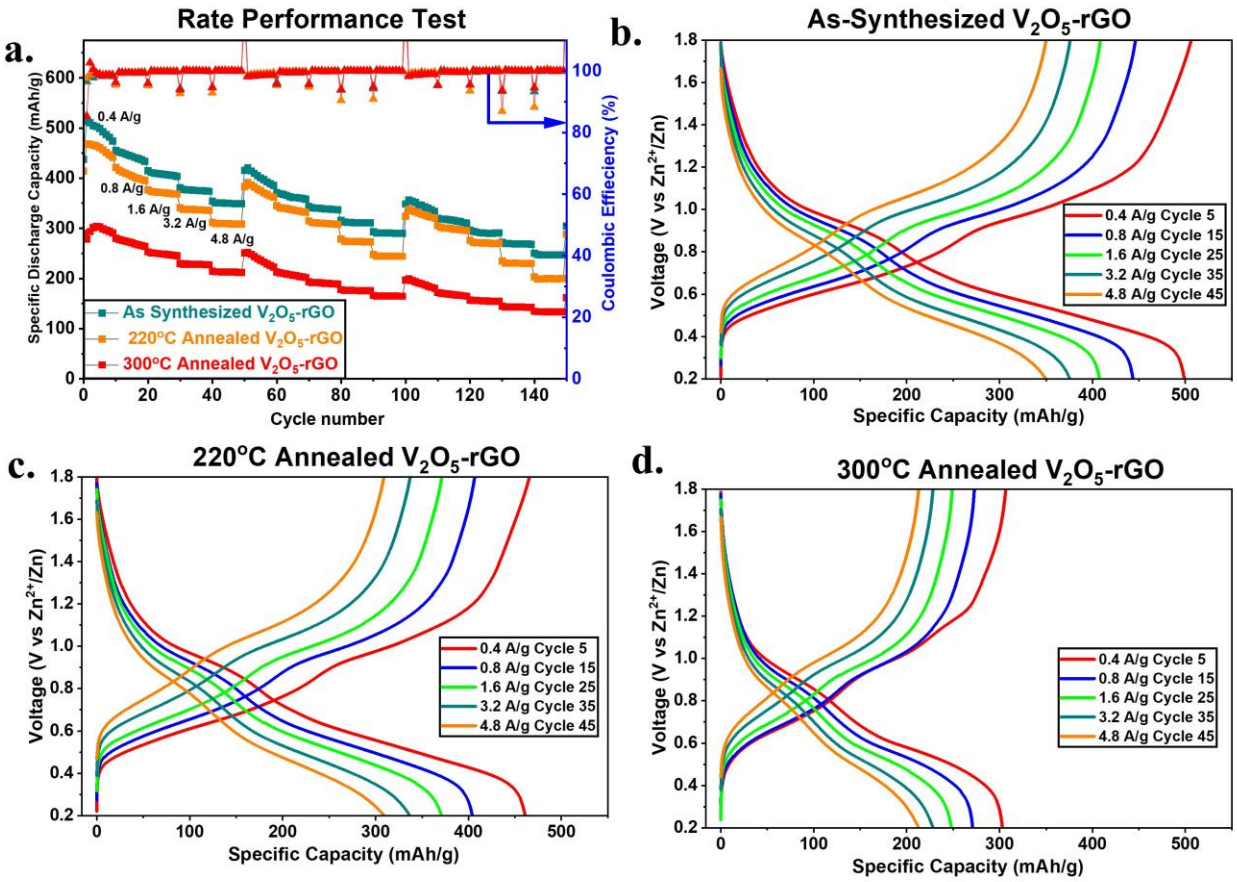

Figure 8 : Galvanostatic charge–discharge performance of V_2O_5–rGO cathodes in aqueous zinc-ion batteries within a potential window of 0.2–1.8 V. (a) Rate performance of as-synthesized, 220 °C annealed, and 300 °C annealed samples at current densities of 0.4, 0.8, 1.6, 3.2, and 4.8 A g^{-1}. (b–d) Corresponding charge–discharge profiles of (b) as-synthesized, (c) 220 °C annealed, and (d) 300 °C annealed samples.

The Zn^{2+} ion storage properties of the as-synthesized V_2O_5-rGO cathode was investigated using galvanostatic charge-discharge tests for rate performance evaluation (Figure 8.) and cycling stability tests (Figure 9). The rate-performance evaluation was carried out between 0.2 V and 1.8 V potential window (with respect to Zn^{2+}/Zn) at current densities of 0.4 A g^{-1}, 0.8 A g^{-1}, 1.6 A g^{-1}, 3.2 A/g and 4.8 A/g (calculated with respect to mass of V_2O_5 only obtained from TGA analysis) with 10 cycles repeated at each current rate. As is evident from Figure 9, as-synthesized V_2O_5-rGO has the highest specific gravimetric capacity. The highest specific capacity of 513 mAh/g was reached in the first cycle decreased with an increase in cycle number, and for higher current

densities they are 499 mAh g^{-1}, 444 mAh g^{-1}, 408 mAh g^{-1} , 376 mAh g^{-1} and 350 mAh g^{-1} (for 5^{th}, 15^{th}, 25^{th}, 35^{th} 45^{th} cycle respectively) which correspond to a capacity retention of 89%, 82%,75%.70% respectively at 0.8 A g^{-1}, 1.6 A g^{-1}, 3.2 A g^{-1} and 4.8 A g^{-1}. When the current density is switched back to 0.4 A g^{-1}, it regains 80 % of its initial capacity (capacity retention calculated with respect of specific capacity of cycle 1.

The 220 °C annealed sample reached the highest capacity of 469 mAh g^{-1} at the first cycle at 0.4 A g^{-1} current density and subsequently 461 mAh g^{-1}, 404 mAh g^{-1}, 371 mAh g^{-1}, 337 mAh g^{-1}, 309 mAh g^{-1} for the 5^{th}, 15^{th}, 25^{th}, 35^{th} and 45^{th} cycle respectively. The capacity retention for it are 88%, 80%,73%.67% respectively at 0.8 A g^{-1}, 1.6 A g^{-1}, 3.2 A g^{-1}, and 4.8 A g^{-1}, and it regains 81 % initial capacity when the current density is turned back to 0.4 A g^{-1}. For 300 °C annealed sample, due to activation process, highest capacity of 304 mAh g^{-1}, is reached in cycle 4 and the consequent specific capacities in 5^{th}, 15^{th}, 25^{th}, 35^{th} 45^{th} cycle are 303 mAh g^{-1} , 271 mAh g^{-1} , 248 mAh g^{-1} , 228 mAh g^{-1}, 213 mAh g^{-1} corresponding to capacity retention of 89 %, 82%, 75% 74% at 0.8 A g^{-1} , 1.6 A/g^{-1} , 3.2 A g^{-1} and 4.8 A g^{-1} and 78% on going back to 0.4 A g^{-1}. This shows that the capacity retention of going from lower to higher current density and switching back to lower current density remains almost unchanged for all three samples. This can probably be attributed to the formation of a hybrid structure with rGO, with the added conductivity or annealed rGO counteracting the effect of slower diffusion, keeping capacity retention the same.

The plateaus on the individual charge-discharge curves for the att three cathode materials (Figure 8. (b. – d.)) correspond well to the peak potentials in CV, indicating consistency in the electrochemical reactions. The presence of distinct plateaus even at higher current densities for as-synthesized and 220 ºC annealed samples shows that diffusion-controlled intercalation occurs even at high current rates. For the 300 ºC annealed sample at higher current densities, the plateaus become less distinct, signaling the increased barrier for Zn^{2+} ions to diffuse into the smaller interlayer spacing of crystalline V_2O_5. Also, the coulombic efficiency is within 99 to 100 % for all three samples, demonstrating excellent reversibility. The specific capacity values exceed the specific capacity of manV_2O_5-rGo and hydrated V_2O_5 materials reported in the literature. (Table 2). However, the material needs to be tested at higher mass loading (2 -3 mg/cm^{-2}) for proper comparison. Another important distinction is the fact that we measure specific capacity with respect to mass of V_2O_5 only, as it enables us to compare the different annealing conditions, which differ in carbon content, while many researchers report specific capacity with respect to total mass

of V_2O_5 and rGO. When compared to literature where only mass of V_2O_5 is considered, it is found that our specific capacity value falls in the reported range. [32]

The cathode materials were tested for cycling stability at two different current densities of 0.4 A g^{-1} and 3.2 A g^{-1}. Testing at low current density (<0.5 A g^{-1}) is important because for grid storage application, batteries should be able to charge and discharge over several hours and supply low current constantly to homes over an extended period of time. For aqueous zinc-ion batteries, due to side reactions like cathode dissolution getting amplified over a long time, over 100 cycles the stability at lower current density is lower than that at higher current density.[33] This is also evident in our research. At 0.4 A g^{-1} the as-synthesized sample retains 54 % of its capacity (530 mAh g^{-1} to 285 mAh g^{-1}) and 31% over 400 cycle (167 mAh g^{-1}) which is slightly higher than that for 220 ºC annealed sample which retains 44 % over 100 cycles and 28 % over 400 cycles (444 mAh g^{-1}, 197 mAh g^{-1}, and 123 mAh g^{-1}) . The 300 ºC annealed sample retains 43 % over 100 cycles and 24 % over 400 cycles (339 mAh g^{-1}, 146 mAh g^{-1}, and 80 mAh g^{-1}). Thus, it is evident that for low current density applications such as grid energy storage the as-synthesized sample is the best contender among the three.

For stability test at 3.2 A g^{-1} the cells were testable upto 1300 cycles compared to only 490 cycles at 0.4 A g^{-1} and showed higher stability as expected. Even at higher current density the as-synthesized sample showed the best performance with 86 %, 55 %, and 45 % capacity retention after 100, 500 and 1000 cycles (464 mAh g^{-1} , 397 mAh g^{-1}, 257 mAh g^{-1}, 208 mAh g^{-1}) . 220 °C annealed cathode retaied 83 %, 51 %, 42% (426 mAh g^{-1} , 353 mAh g^{-1}, 219 mAh g^{-1}, 179 mAh g^{-1}) and 300 °C annealed samples retained 84 %, 55% and 40% respectively (287 mAh g^{-1}, 241 mAh g^{-1}, 158 mAh g^{-1}, 115 mAh g^{-1}).

The stability is much lower than that reported in the literature for similar material. Possible reasons for that could be lower mass loading, which amplifies the effect of cathode dissolution, and the use of the full potential window, which causes side reactions such as HER and OER (Table

2).

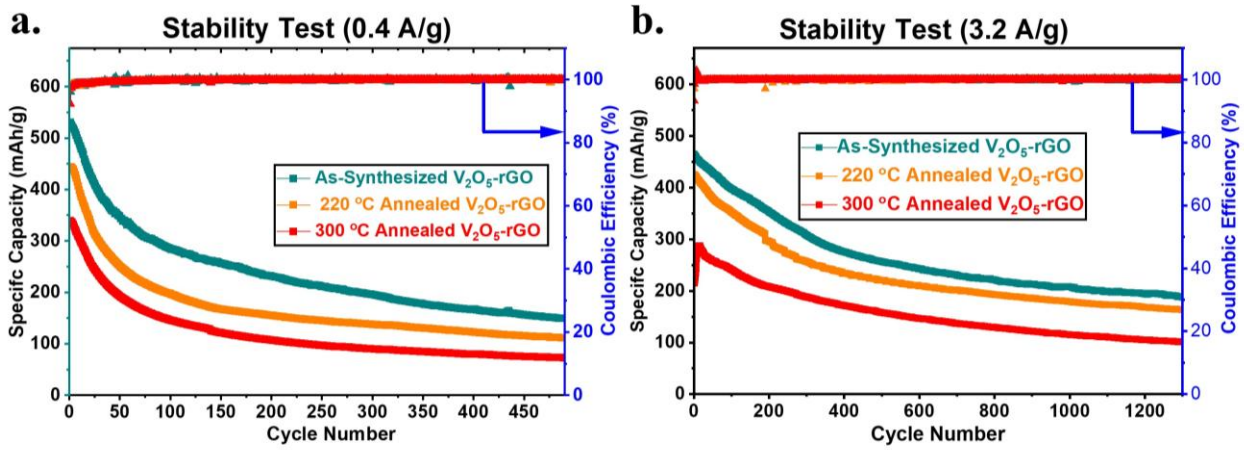

Figure 9 : Cycling stability of V_2O_5–rGO cathodes in aqueous zinc-ion batteries within a potential window of 0.2–1.8 V of the as-synthesized, 220 °C annealed, and 300 °C annealed samples at current densities of (a) 0.4 A g^{-1} and (b) 3.2 A g^{-1}.

Table 2 : Comparison of the synthesis method and electrochemical performance of hydrated vanadium pentoxide-based materials as the cathode for zinc ion batteries**.**

Material	Synthesis Method	Mass Loading (mg/cm^{-2})	Highest Specific Capacity	Stability (Capacity retention)	Potential window (V vs Zn^{2+}/Zn)	Annealing	Ref
V_2O_5-rGO	Sol-gel	2.5	381 mAh g^{-1} at 0.6 A g^{-1}	71 % after 900 cycles at 6 A g^{-1}	0.2 – 1.6 V	Not annealed	8
V_2O_5-EGO	Melt quenching, EGO = electrochemically produced graphene oxide	1	462 mAh g^{-1} at 0.6 A g^{-1}	67.5% after 1000 cycles at 5A g^{-1}	0.2 – 1.6 V	Not annealed (Spray-dried at 200 °C	18

V_2O_5-rGO	Hydrothermal	1.7 -2.0	311 mAh g^{-1} at 0.1 A g^{-1}	87% after 100 cycles at 0.1 A g^{-1}	0.2 – 1.6 V	350 °C for 0.5 hours	9
Hydrated V_2O_5 nanoflake	Sol-gel (H_2O_2 digestion)	1	346.6 mAh g^{-1} at 0.1 A g^{-1}	61 % after 1800 cycles at 1 A g^{-1}	0.2-1.5 V	Not annealed	34
V_2O_5-rGO	Melt- quenching	2.3	496 mAh g^{-1} at 0.1 A g^{-1}	85 % after 3800 cycles at 5 A g^{-1}	0.3-1.6 V	Not annealed	35
V_2O_5-rGO	Microwave	0.6 -0.9	513 mAh g^{-1} at 0.4 A g^{-1}	45 % after 1000 cycles at 3.2 A g^{-1} 54 % after 100 cycles at 0.4 A g^{-1}	0.2 – 1.8 V	Not annealed	This work

Chapter 4 - Conclusion

In summary, hybrid material with hydrated V_2O_5 anchored to rGO was successfully synthesized with microwave assisted method using vanadium(V) oxytriisopropoxide and GO that reduced the total synthesis time to 10 minutes, which is significantly shorter than conventional ambient-pressure techniques and hydrothermal techniques. The as-synthesized product was annealed at 220 °C and 300 °C to study the effect of annealing on its electrochemical properties.

Raman spectroscopy confirmed the formation of hybrid structure including both V_2O_5 and GO and hinted at increase in crystallinity and loss of intercalated water with annealing, X-ray diffraction demonstrated the structure of the as-synthesized and 220 °C annealed samples being amorphous bilayer V_2O_5 structure with the annealed sample having less interlayer spacing and 300 °C annealed sample as crystalline α-V_2O_5 structure. Thermogravimetric analysis was used to estimate relative amount of V_2O_5 and rGO in hybrid samples, demonstrating reduction of rGO amount on annealing reducing to nearly 10% on annealing at 300 ºC.

On electrochemical testing as-synthesized sample shows the highest specific capacity of 513 mAh g^{-1} corresponding to Zn^{2+} insertion per V_2O_5 unit and decreases monotonically with increase in annealing temperature. Cyclic voltammetry showed low energy barrier to Zn^{2+} insertion and extraction for as-synthesized sample. Cycling stability and rate capability remained similar for annealed and as synthesized samples. On comparing with literature (Table 2), the specific capacity is on the high end of reported values while the cycling stability of 54 % capacity retention after 100 cycles and 45 % retention after 1000 cycles at 0.4 and 3.2 A g^{-1} significantly fall short of stability of materials reported in literature. The primary reason for this could be the low mass loading (0.6 to 0.9 mg/cm^{-2}) used compared to more practical mass loadings of 2 – 3 mg/ cm^{-2} used

in literature (Table 2) which would reduce the specific capacity observed due to all the material not participating but reduce capacity fading due to cathode dissolution as dissolving of cathode would just expose more material that can still function.

Ways to improve the cycling stability might include better studying of the mechanisms that lead to capacity fading like cathode dissolution and hydrogen evolution, reducing potential window to reduce side reactions at extreme voltages, using electrolyte additives and water in salt electrolytes ton reduce side reactions.

Overall, the as-synthesized V_2O_5-rGO hybrid material synthesized via microwave irradiation can act as a promising candidate for future aqueous zinc-ion batteries, however, poor cycling stability needs to be addressed before it becomes a viable cathode material.

References

(1) Yolcan, O. O. World energy outlook and state of renewable energy: 10-Year evaluation. *Innovation and Green Development* **2023**, *2* (4), 100070.
(2) Yang, Z.; Zhang, J.; Kintner-Meyer, M. C. W.; Lu, X.; Choi, D.; Lemmon, J. P.; Liu, J. Electrochemical Energy Storage for Green Grid. *Chemical Reviews* **2011**, *111* (5), 3577-3613.
(3) Jia, X.; Liu, C.; Neale, Z. G.; Yang, J.; Cao, G. Active Materials for Aqueous Zinc Ion Batteries: Synthesis, Crystal Structure, Morphology, and Electrochemistry. *Chemical Reviews* **2020**, *120* (15), 7795-7866.
(4) Zhang, W.; Xiong, T.; Qiu, X. Electrolyte engineering for future aqueous Zn-ion batteries. *Cell Reports Physical Science* **2025**, *6* (10), 102853.
(5) Zhang, Y. C.; Ji, X. Y.; Xie, C. D.; Yang, R.; Zhang, F.; Tang, Y. B. Aqueous Secondary Batteries: Status and Challenges. *Energy Storage Materials* **2025**, *77*, 104186.
(6) Muthukumar, K.; Rajendran, S.; Sekar, A.; Chen, Y.; Li, J. Synthesis of V_2O_5 Nanoribbon–Reduced Graphene Oxide Hybrids as Stable Aqueous Zinc-Ion Battery Cathodes via Divalent Transition Metal Cation-Mediated Coprecipitation. *ACS Sustainable Chemistry & Engineering* **2023**, *11* (6), 2670-2679.
(7) Yin, C.; Li, L.; Hu, J. Intercalating polypyrrole tuning interlayer space of V_2O_5 for advanced aqueous zinc ion batteries. *Colloids and Surfaces A: Physicochemical and Engineering Aspects* **2024**, *692*, 134013.
(8) Yan, M.; He, P.; Chen, Y.; Wang, S.; Wei, Q.; Zhao, K.; Xu, X.; An, Q.; Shuang, Y.; Shao, Y.; et al. Water-Lubricated Intercalation in $V_2O_5{\cdot}nH_2O$ for High-Capacity and High-Rate Aqueous Rechargeable Zinc Batteries. *Advanced Materials* **2018**, *30* (1), 1703725.
(9) Liu, T.; Xu, Z.; Chen, L.; Zhang, Y.; Wang, M.; Jia, Y.; Huang, Y. Boosting zinc ion storage performance of sandwich-like V_2O_5/graphene composite by effectively inhibiting vanadium dissolution. *Journal of Colloid and Interface Science* **2022**, *613*, 524-535.
(10) Aniskevich, Y.; Myung, S.-T. Gains and losses in zinc-ion batteries by proton- and water-assisted reactions. *Chemical Society Reviews* **2025**, *54* (9), 4531-4566, 10.1039/D4CS00810C.
(11) Sun, W.; Wang, F.; Hou, S.; Yang, C.; Fan, X.; Ma, Z.; Gao, T.; Han, F.; Hu, R.; Zhu, M.; et al. Zn/MnO2 Battery Chemistry With H^+ and Zn^{2+} Coinsertion. *Journal of the American Chemical Society* **2017**, *139* (29), 9775-9778.
(12) Wang, B.; Xu, H.; Hao, J.; Du, J.; Wu, C.; Ma, Z.; Qin, W. Mini-Review on the Regulation of Electrolyte Solvation Structure for Aqueous Zinc Ion Batteries. *Batteries* **2023**, *9* (2), 73.
(13) Livage, J. Vanadium pentoxide gels. *Chemistry of Materials* **1991**, *3* (4), 578-593.
(14) Petkov, V.; Trikalitis, P. N.; Bozin, E. S.; Billinge, S. J. L.; Vogt, T.; Kanatzidis, M. G. Structure of $V_2O_5{\cdot}nH_2O$ Xerogel Solved by the Atomic Pair Distribution Function Technique. *Journal of the American Chemical Society* **2002**, *124* (34), 10157-10162.
(15) Li, H.; He, P.; Wang, Y.; Hosono, E.; Zhou, H. High-surface vanadium oxides with large capacities for lithium-ion batteries: from hydrated aerogel to nanocrystalline VO_2(B), V_6O_{13} and V2O5. *Journal of Materials Chemistry* **2011**, *21* (29), 10999-11009, 10.1039/C1JM11523E.
(16) Li, J.; Li, Y.; Yao, J.; Huang, B.; Jiang, J.; Yang, J. Effect of heat treatment on the electrochemical performance of $V_2O_5{\cdot}nH_2O$ as a cathode material for aqueous rechargeable zinc ion batteries. *Journal of Industrial and Engineering Chemistry* **2022**, *115*, 554-560.

(17) Gnanasekar, S.; Sonar, P.; Jain, S. M.; Jeong, S. K.; Grace, A. N. Performance evaluation of a low-cost, novel vanadium nitride xerogel (VNXG) as a platinum-free electrocatalyst for dye-sensitized solar cells. *RSC Advances* **2020**, *10* (67), 41177-41186, 10.1039/D0RA06984A.
(18) Zhang, Y.; Qin, J.; Batmunkh, M.; Li, W.; Fu, H.; Wang, L.; Al-Mamun, M.; Qi, D.; Liu, P.; Zhang, S.; et al. Scalable Spray Drying Production of Amorphous V_2O_5–EGO 2D Heterostructured Xerogels for High-Rate and High-Capacity Aqueous Zinc Ion Batteries. *Small* **2022**, *18* (10), 2105761.
(19) Pandey, G. P.; Liu, T.; Brown, E.; Yang, Y.; Li, Y.; Sun, X. S.; Fang, Y.; Li, J. Mesoporous Hybrids of Reduced Graphene Oxide and Vanadium Pentoxide for Enhanced Performance in Lithium-Ion Batteries and Electrochemical Capacitors. *ACS Applied Materials & Interfaces* **2016**, *8* (14), 9200-9210.
(20) Moretti, A.; Maroni, F.; Osada, I.; Nobili, F.; Passerini, S. V2O5 Aerogel as a Versatile Cathode Material for Lithium and Sodium Batteries. *ChemElectroChem* **2015**, *2* (4), 529-537.
(21) Wen, B.; Wang, X. X.; Cao, W. Q.; Shi, H. L.; Lu, M. M.; Wang, G.; Jin, H. B.; Wang, W. Z.; Yuan, J.; Cao, M. S. Reduced graphene oxides: the thinnest and most lightweight materials with highly efficient microwave attenuation performances of the carbon world. *Nanoscale* **2014**, *6* (11), 5754-5761.
(22) Gabriel, C.; Gabriel, S.; H. Grant, E.; H. Grant, E.; S. J. Halstead, B.; Michael P. Mingos, D. Dielectric parameters relevant to microwave dielectric heating. *Chemical Society Reviews* **1998**, *27* (3), 213-224, 10.1039/A827213Z.
(23) Shvets, P.; Maksimova, K.; Goikhman, A. In situ XRD and Raman study of the phase transition in V2O5 xerogels. *Journal of Non-Crystalline Solids* **2024**, *625*, 122751.
(24) Castriota, M.; Cazzanelli, E.; Fasanella, A.; Teeters, D. Electrical conductivity and Raman characterization of V_2O_5 grown by sol–gel technique inside nanoscale pores. *Thin Solid Films* **2014**, *553*, 127-131.
(25) Lee, S.-H.; Cheong, H. M.; Seong, M. J.; Liu, P.; Tracy, C. E.; Mascarenhas, A.; Pitts, J. R.; Deb, S. K. Raman spectroscopic studies of amorphous vanadium oxide thin films. *Solid State Ionics* **2003**, *165* (1), 111-116.
(26) Brown, E.; Acharya, J.; Pandey, G. P.; Wu, J.; Li, J. Highly Stable Three Lithium Insertion in Thin V_2O_5 Shells on Vertically Aligned Carbon Nanofiber Arrays for Ultrahigh-Capacity Lithium Ion Battery Cathodes. *Advanced Materials Interfaces* **2016**, *3* (23), 1600824.
(27) Yu, S.; Zhang, X.; Zhan, Q.; Yu, H.; Zhou, B. A comparative theoretical study on the vibrational spectra of V_2O_5·nH2O. *Physical Chemistry Chemical Physics* **2026**, *28* (6), 4229-4241, 10.1039/D5CP04227E.
(28) Aliyev, E.; Filiz, V.; Khan, M. M.; Lee, Y. J.; Abetz, C.; Abetz, V. Structural Characterization of Graphene Oxide: Surface Functional Groups and Fractionated Oxidative Debris. *Nanomaterials* **2019**, *9* (8), 1180.
(29) Wu, S.; Liu, S.; Hu, L.; Chen, S. Constructing electron pathways by graphene oxide for V2O5 nanoparticles in ultrahigh-performance and fast charging aqueous zinc ion batteries. *Journal of Alloys and Compounds* **2021**, *878*, 160324.
(30) Li, R.; Zhang, H.; Zheng, Q.; Li, X. Porous V_2O_5 yolk–shell microspheres for zinc ion battery cathodes: activation responsible for enhanced capacity and rate performance. *Journal of Materials Chemistry A* **2020**, *8* (10), 5186-5193, 10.1039/C9TA11750D.
(31) Hu, Z.; Meng, D.; Wu, Y.; Huang, Y.; Li, L.; Hong, Z. Activation and degradation mechanisms of α-V_2O_5 cathode materials in Zn-ion battery. *Journal of Power Sources* **2024**, *604*, 234465.

(32) Chi, J.; Xu, H.; Wang, J.; Tang, X.; Yang, S.; Ding, B.; Dou, H.; Zhang, X. In Situ Electrochemically Oxidative Activation Inducing Ultrahigh Rate Capability of Vanadium Oxynitride/Carbon Cathode for Zinc-Ion Batteries. *ACS Applied Materials & Interfaces* **2023**, *15* (3), 4061-4070.
(33) Liu, S.; Zhang, R.; Wang, C.; Mao, J.; Chao, D.; Zhang, C.; Zhang, S.; Guo, Z. Zinc ion Batteries: Bridging the Gap from Academia to Industry for Grid-Scale Energy Storage. *Angewandte Chemie International Edition* **2024**, *63* (17), e202400045.
(34) Guo, K.; Cheng, W.; Chen, H.; Li, H.; Chen, J.; Liu, H.; Tu, Y.; She, W.; Huang, Z.; Wan, Y.; et al. Facile and Rapid Synthesis of Porous Hydrated V_2O_5 Nanoflakes for High-Performance Zinc Ion Battery Applications. *Nanomaterials* **2022**, *12* (14), 2400.
(35) Wei, T.; Li, Q.; Yang, G.; Wang, C. Pseudo-Zn–Air and Zn-Ion Intercalation Dual Mechanisms to Realize High-Areal Capacitance and Long-Life Energy Storage in Aqueous Zn Battery. *Advanced Energy Materials* **2019**, *9* (34), 1901480.